Earthquake Research Advances xxx (xxxx) xxx

Contents lists available at ScienceDirect

Earthquake Research Advances

journal homepage: www.keaipublishing.com/en/journals/earthquake-research-advances

Detailed sedimentary structure of the Mianning segment of the Anninghe fault zone revealed by H/V spectral ratio

Zeqiang Chen [a], Huajian Yao [a,b,c,*], Xihui Shao [a], Song Luo [a], Hongfeng Yang [d,e]

[a] Laboratory of Seismology and Physics of Earth's Interior, School of Earth and Space Sciences, University of Science and Technology of China, Hefei, 230026, China
[b] Mengcheng National Geophysical Observatory, University of Science and Technology of China, Mengcheng, 233500, China
[c] CAS Center for Excellence in Comparative Planetology, University of Science and Technology of China, Hefei, 230026, China
[d] Earth System Science Programme, Faculty of Science, The Chinese University of Hong Kong, Hong Kong, 999077, China
[e] Shenzhen Research Institute, The Chinese University of Hong Kong, Shenzhen, 518057, China

ARTICLE INFO

Keywords:
HVSR
Shallow structure
Anninghe fault zone
Sediment
Earthquake hazard prevention

ABSTRACT

The Anninghe fault is a major left-lateral strike-slip fault in southwest China and a seismic gap with a potential earthquake larger than M_W7.0 lies in the Mianning-Xichang segment according to recent observations. The shallow structure of this region can offer a glimpse into the geometry of the fault, which plays an important role in earthquake hazard mitigation. To further investigate the sedimentary structure of the Anninghe fault zone, two dense linear arrays with a station spacing of around 80 m were deployed across the fault. In this study, the H/V spectral ratio (HVSR), together with its peak frequency at each station site, was obtained by applying the Nakamura method. Our findings demonstrate that the peak frequency behaves in high correlation with lithology and is controlled by topography. HVSR in foothills or regions with magmatic intrusion shows a single peak at about 2–3 Hz. In locations with abundant Quaternary sedimentation, such as Anninghe valleys and fracture zones, another low-frequency peak around 0.4 Hz can be noticed in HVSR. By using the empirical relationship, the thickness of the sedimentary layer around the fault fracture zone is estimated to be 300–600 m. Furthermore, the sedimentary interface shows a downward dip to the east, possibly influenced by the east-west extrusion stress. Considering the resonance effect, buildings with 6–9 stories in the valley area of the Anninghe require additional attention in earthquake hazard prevention.

1. Introduction

The Anninghe fault forms the northeast boundary of the Sichuan-Yunnan rhomboidal block in Southwest China. As a major left-lateral strike-slip fault, it intersects with the Xianshuihe fault in the north and the Zemuhe fault in the south, spanning almost 200 km. The seismic activity of the Anninghe fault is very intense (Zhang, 2008) due to the eastward material extrusion from the Tibetan Plateau and the obstruction of the Sichuan Basin (King et al., 1997; Chen et al., 2000; Zhang et al., 2004, 2010). There have been a number of significant earthquakes in history, including the 1480 $M7^1/_2$, 1536 $M7^1/_2$, 1913 $M6$, and 1952 $M6^3/_4$ (Wen, 2000; Wen et al., 2007). However, the distribution of $M_L \geq 2.5$ earthquakes in the region over the past 40 years indicates that there is a clear seismic gap between the Liziba (north of Mianning) to Xichang segment of the Anninghe fault zone (Wen et al., 2008a, 2008b). According to Wen et al. (2008a), this region exhibits a high locking characteristic and has undergone significant strain accumulation. They concluded that the highest magnitude of the probable earthquake would be M_W7.4, which greatly arouse the attention of the field.

Previous studies mainly focused on large-scale seismic imaging of this area, including surface wave tomography (Yao et al., 2006, 2008; Zhang et al., 2020), receiver functions (Xu et al., 2007; Zhang et al., 2010; Hu

* Corresponding author. Laboratory of Seismology and Physics of Earth's Interior, School of Earth and Space Sciences, University of Science and Technology of China, Hefei, 230026, China.
E-mail address: hjyao@ustc.edu.cn (H. Yao).

Production and Hosting by Elsevier on behalf of KeAi

https://doi.org/10.1016/j.eqrea.2023.100232
Received 16 November 2022; Received in revised form 15 April 2023; Accepted 18 April 2023

Please cite this article as: Chen, Z. et al., Detailed sedimentary structure of the Mianning segment of the Anninghe fault zone revealed by H/V spectral ratio, Earthquake Research Advances, https://doi.org/10.1016/j.eqrea.2023.100232

et al., 2018), and joint inversion (Liu et al., 2014; Bao et al., 2015; Yang et al., 2020). Liu et al. (2021) integrated body wave and surface wave travel time data to establish the first Community Velocity Model (CVM) for the Sichuan-Yunnan region, while Shao et al. (2022) obtained three P-wave velocity profiles in the shallow crust across the Anninghe fault zone using a methane gas active source, and Luo et al. (2023) obtained the 3-D Vs model of the shallow crust in the southern part of the Anninghe fault zone from ambient noise tomography. These velocity models characterize the structure of the Anninghe fault to some extent, but the large-scale structural models with a lateral resolution of more than tens of kilometers make it challenging to figure out the details of this seismic gap, let alone the information about the interface. Wang et al. (1998) obtained the lithologic distribution and stratigraphic table within the fault zone through field geological surveys. He and Yasutakyr (2007) further proposed the existence of asymmetry on both sides of the fault zone by combining aerial images and pointed out that the lower plate of the Anninghe fault plunges to the south-east. This geological information does strengthen our understanding of the shallow structure in the area, but because of the limitation of the geological investigation on sparse locations, the continuity of the fault zone still remains poorly understood.

The microtremor H/V spectral ratio (HVSR) method is commonly used to study the characteristics of sediments and site response, which can provide a crucial foundation for strong ground motion simulations and earthquake rupture studies (Zhang et al., 2015; Hu et al., 2022). Although the principle of HVSR is still up for debate, it is widely acknowledged that the peak frequency is related to the thickness of subsurface interfaces (e.g., sediment layers) (Nakamura, 1989; Ibs-von Seht and Wohlenberg, 1999; Wang et al., 2011; Tun et al., 2016; Bao et al., 2018), and can be further applied to study the site amplification effect or earthquake hazard prevention (Bard, 1999; Panou et al., 2005; Mokhberi, 2015; Zhang et al., 2015; Guven, 2022). With the development of portable seismometers, the HVSR technique has gradually become a popular tool to retrieve information about shallow-subsoil seismic properties with its low cost and high time efficiency compared with traditional borehole logging (Panou et al., 2005; Hu et al., 2022; Vassallo et al., 2022).

To better characterize the shallow structure of the seismic gap of the Anninghe fault zone, we collected ambient noise data recorded by the two linear arrays deployed right across the central Anninghe fault zone. By applying the H/V spectral ratio method, two peak frequency profiles with a spatial resolution of 80 m were achieved. Afterward, two empirical formulas were adopted with the aim to determine the sedimentary interface depths including the uncertainty from peak frequency. Furthermore, we presented the correlation between peak frequency, topography, lithology, and velocity. In addition, we tried to figure out the geometry of sediment in the vicinity of the fault fracture zone. Finally, we discussed the earthquake hazard prevention of surrounding buildings and some suggestions are given according to the resonant frequency.

2. Data and method

2.1. Data acquisition and preprocessing

In this study, two linear arrays (Fig. 1b) were deployed in the area with dense populations along the valley of the Anninghe fault, and a total of 217 three-component short-period sensors (QS-05: 5 s–250 Hz and QS-10: 10 s–250 Hz, using GPS satellite timing) were used. From north to south, Line1 (AL001-AL150) contained 129 seismographs and Line2 (AL201-AL308) contained 88 instead. Both two lines were deployed nearly east-west-oriented with a station spacing of about 80 m and 8 km spanning, crossing the whole Anninghe valley. The array worked from mid-October 2019 to February 2020 with an average continuous recording time of approximately three months. Preprocessing was carried out first on the data including de-meaning, de-trending, and de-spiking. In order to improve the signal-to-noise ratio and obtain clearer HVSR curves, only recordings from 01:00 a.m. to 05:00 a.m. were selected and

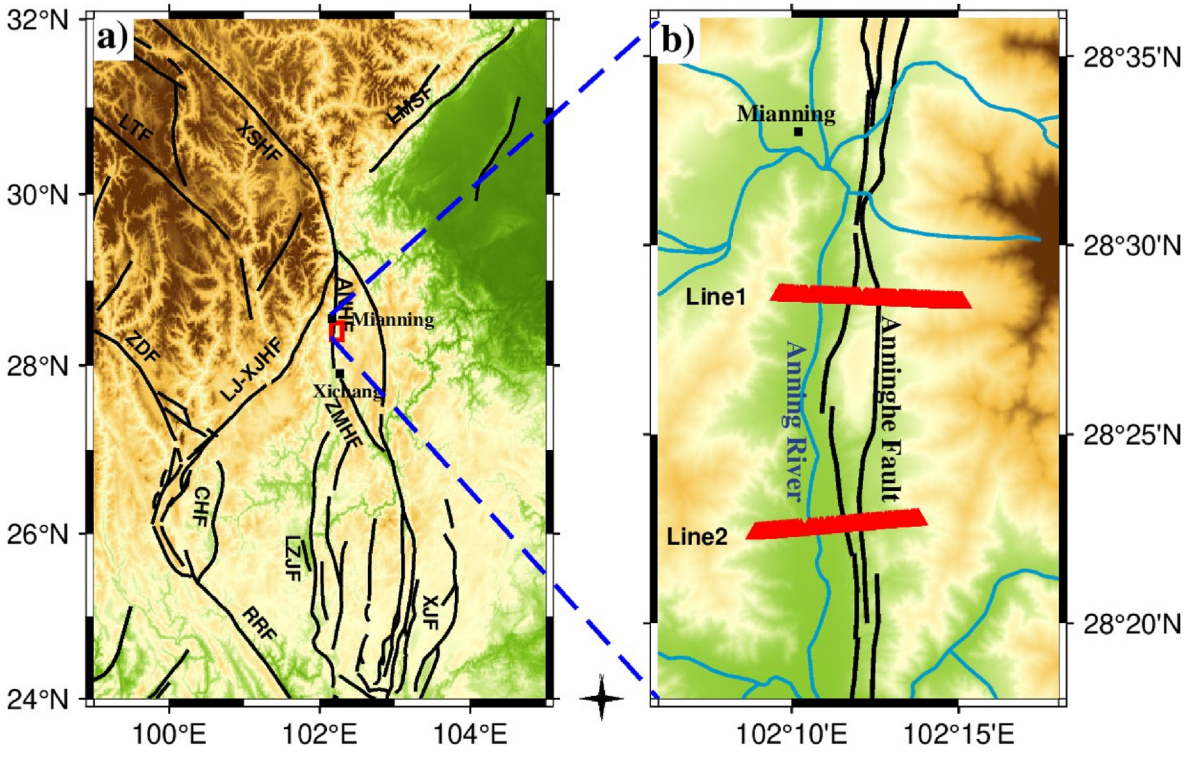

Fig. 1. Tectonics, topography, and array station distribution maps of the Anninghe fault zone and its surrounding areas. (a) Tectonic map showing the active faults in the eastern Qinghai-Tibetan Plateau and the location of the seismic survey area (red rectangle). (b) Distribution of stations (red triangles), cities, faults, and rivers. LTF: Litang Fault, XSHF: Xianshuihe fault, LMSF: Longmenshan fault, ANHF: Anninghe fault, ZDF: Zhongdian fault, LJ-XJHF: Lijiang-Xiaojinhe fault, ZMHF: Zemuhe fault, CHF: Chenghai fault, LZJF: Lüzhijiang fault, RRF: Red River fault, XJF: Xiaojiang fault.

then sliced into 100-sec windows (Fig. 2a). The STA-LTA algorithm (Jones and van der Baan, 2015) was applied to eliminate the influence of transient signals like seismic events, which minimized the interference of artificial noise and greatly improved the quality of data.

2.2. Calculation of HVSRs

The H/V spectral ratio method, also known as Nakamura's method (Nakamura, 1989), is an empirical technique for the estimation of subsurface sediment and has been widely used in geophysical studies. Although part of the theoretical interpretation is not yet clear, there is no doubt that the peak frequency of the HVSR curve can provide information on the thickness of subsurface sedimentary layers (Molnar et al., 2022). Based on Nakamura (1989), assuming that the horizontal and vertical recording spectra of the soft soil layer and bedrock are H_f, V_f, H_b and V_b respectively, then the amplification factor of the soft soil layer on the horizontal component can be stated as $A = H_f/H_b$. Since the horizontal-to-vertical-motion spectral ratio of hard ground H_b/V_b is almost 1 for a wide frequency range based on observations. The amplification characteristics can be rewritten as:

$$\mathrm{HVSR}(f) = \frac{H_f}{H_b}\cdot\frac{V_b}{V_f} = \frac{H_f}{V_f} = \sqrt{\frac{EW^2(f) + NS^2(f)}{2V^2(f)}} \tag{2-1}$$

where EW and NS represent the east-west and north-south components, respectively. The entire workflow can be summarized as follows.

1) For one station, cut three-component noise data recorded from 01:00 a.m. to 05:00 a.m. with a sampling rate of 100 Hz and a total of 144 000 points.
2) The recordings were then sliced into many segments with 100-s lengths and 30% overlapped (Fig. 2a). Each segment was checked based on the STA/LTA algorithm and poor data was discarded.
3) Spectra of the three-component data were calculated separately on each segment (Fig. 2b) and further smoothed by the Konno and Ohmachi (1998) smoothing algorithm.
4) The H/V spectral ratio was computed and stacked to generate the final curve (Fig. 2d). Afterward, the peak frequency was picked based on the SESAME criteria (Acerra et al., 2004) and its continuity of adjacent stations.
5) Switch to the next station and repeat step 1).

2.3. Sedimentary depth conversion and its uncertainty

It is a common practice to pick the peak frequency from the HVSR curves and convert it to sedimentary depth beneath the station (Ibs-von Seht and Wohlenberg, 1999; Wang et al., 2011; Tun et al., 2016). If the shallow S-wave velocity in the area is known, the quarter-wavelength method can be used (Nakamura, 1989; Lachet and Bard, 1994), which is given as follows:

$$H = \frac{V_s}{4f} \tag{2-2}$$

where H, V_s, and f represent the thickness of the sediment, the average subsurface S-wave velocity, and the peak frequency, respectively. It is difficult to constrain the shallow surface S-wave velocity due to the lack of borehole data in the Anninghe fault zone. Numerous observations show that the S-wave velocity is typically around 250 m/s for the shallowest region of the subsurface (Li et al., 2016; Tun et al., 2016; Zhu et al., 2018). Hence, we adopted this value along with some perturbations to represent the average S-wave velocity for the depth estimation of shallow subsurface sediment.

For areas such as river valleys and fracture zones, the sediment thickness may range from hundreds of meters to even 1 km. In such cases, the velocity may not always vary linearly with depth making it inappropriate to use Equas. (2-3) for estimation. It could be more reasonable to use the following empirical relationship in an exponential form:

$$H = af^{-b} \tag{2–3}$$

where f is the peak frequency and a and b are the coefficients to be determined. This relationship was first proposed by Ibs-von Seht and

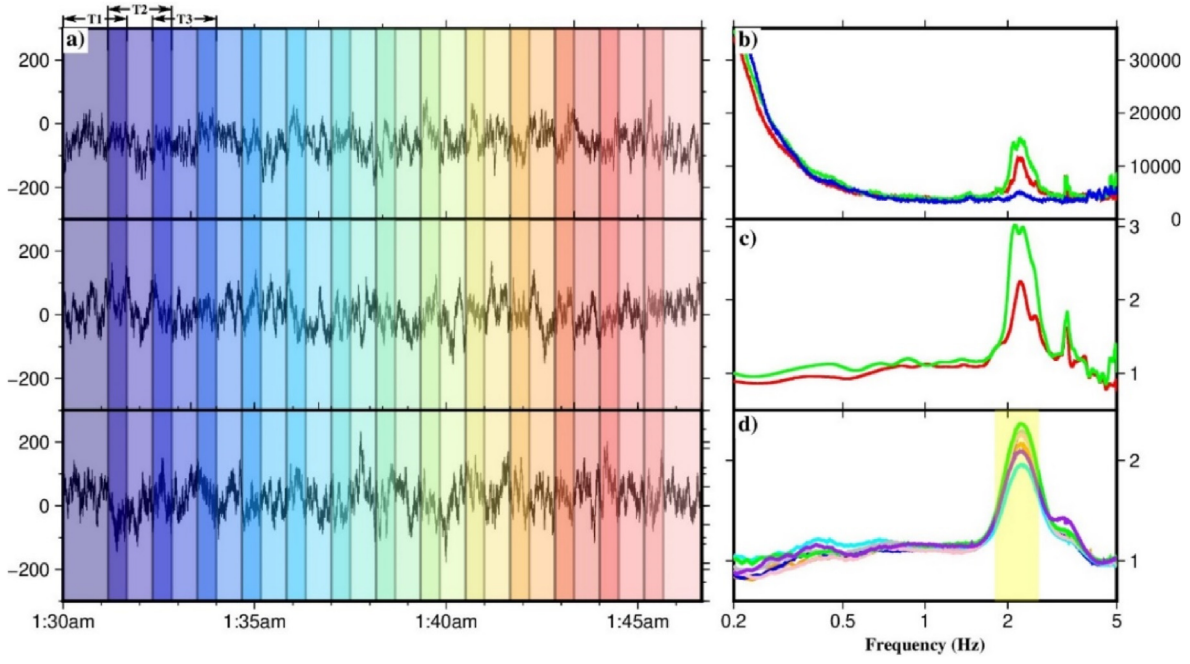

Fig. 2. Example of HVSR processing flow, taking station AL202 for instance. (a) Windowing of microtremor time series. T1, T2, and T3 represent the time windows with 100 s long and 30% overlap. (b) Time window-averaged Fourier amplitude spectra (FAS) for each of the three components. (c) The spectral ratio of the NS component and EW component versus the vertical component. (d) HVSR curves of all days for station AL202. The green, red, and blue line represents the EW, NS, and vertical component, respectively in (b) and (c). Yellow block highlights the peak frequency in (d) and the FASs have been smoothed (Konno and Ohmachi, 1998).

Wohlenberg (1999) and then applied to the German region. Two coefficients are derived from the fitting of the sediment thickness from boreholes to the peak frequency, so the accuracy is guaranteed for the same area or areas with similar lithology. Although there are differences in the coefficients derived by different researchers, the converted results are generally close to each other.

To better constrain the converted depth information, we try to evaluate the uncertainty of the converted depth. For the shallower interface converted using Equas. (2-2), the error arises from the uncertainty of the average S-wave velocity and the peak frequency. The former part can be obtained by setting a velocity range while the latter can be achieved by statistical analysis of all the HVSR curves for one station, which can be obtained from the frequency range of the peak frequency within a specific confidence interval (Fig. A1). As for the deeper interfaces derived from Equas. (2-3), besides the uncertainty of peak frequency itself, it depends on the coefficients which can be obtained by employing the results of different studies.

3. Results

Based on the method mentioned before, we finally obtained the H/V spectral ratio of all stations with frequencies between 0.2 and 50 Hz. Few peaks over 5 Hz can be seen, with the majority of peak frequencies being between 0.2 and 5 Hz (Fig. A2). Statistical analysis shows that their characteristics may be categorized into three groups: single-peak (Fig. 3a and d), multi-peaks (Fig. 3b and e), and no-peak (Fig. 3c and f). Peak frequencies can be selected among 179 stations, with only 38 stations lacking a visible peak in their HVSR curves (Fig. 3g). A single peak implies the existence of a strong impedance contrast in the subsurface, and the peak frequency at this time is approximately the resonant frequency of the sedimentary layer. The reason for multi-peaks is still unclear, one possible explanation for this might be the existence of multiple impedance contrasts (Bodin et al., 2001). We notice that there are some stations without peak frequency which may be resulted from poor data or the absence of a sharp interface beneath the stations (Wang et al., 2011).

The HVSR curves were normalized and then arranged by distance for a better understanding of the characteristics. Fig. 4 shows the peak frequencies of both lines have good continuity. There is a global high-frequency peak of around 3 Hz in Line 1, while the HVSR curves at most stations at 0.5–2 km and 5–7 km show double peaks with a low-frequency peak of around 0.5 Hz in addition to the high-frequency peak around 3 Hz. The characteristics of the HVSR curves of Line 2 are much clearer (Fig. 4) and from the beginning of the left side to a distance of about 2 km, the peak frequency decreases continuously from 2 Hz to 1 Hz, while double peaks start to appear at 1 km. The peak frequency drops steadily to 0.4 Hz till 5 km after a small jump to 2 Hz at 2 km, and the HVSR curves occasionally show multi-peaks at a distance of 4–5 km. After 5 km, the HVSRs become complex with some stations having multi-peaks and the overall peak frequency starts to increase gradually.

We further picked the peak frequency of the HVSR curves as well as the amplitude based on the quality of the peak frequency and its continuity of the adjacent stations, as shown in Fig. 5. Line1's elevation difference is over 500 m and both its east and west sides as well as the central part (4–5 km) are mountains. The peak frequencies of the mountainous areas on both sides are around 2Hz while stations on the west side have double peaks with H/V amplitudes of about 2, and the peak frequency seems to decrease with increasing distance. On the contrary, the peak frequency on the east side is relatively smooth and dominated by a single peak with an H/V amplitude of 1.5 or less. In the river valley area on the west side (1–4 km), the larger peak at around 2–3 Hz vanishes from 2 km to 3 km and is replaced by a lower frequency peak of about 0.5 Hz with an amplitude of 1.5–2. The frequencies exhibit double peaks when stations approach the east side of the valley (5–7 km), with one peak occurring at about 2–3 Hz and the other at about 0.5 Hz, both with a H/V amplitude of about 1.5. There are even some peak frequencies greater than 5 Hz at 6.5 km. The central mountainous area located between those two valleys has a high-frequency peak with a H/V amplitude of about 2.5, which is obviously larger than the two sides. The elevation of Line 2 (Fig. 5b) changes a little compared with Line 1 and the peak frequencies gradually decrease from 2 Hz (0 km) to 0.3 Hz (5 km) with a H/V amplitude of 2.5. It's not surprising to find that HVSRs become complex in the area where the Anninghe passes through (1–2.5 km) as well as the fault fracture zone (4–5 km). Multi-peaks begin to dominate the HVSR curves and an inverted trapezoid is formed by the

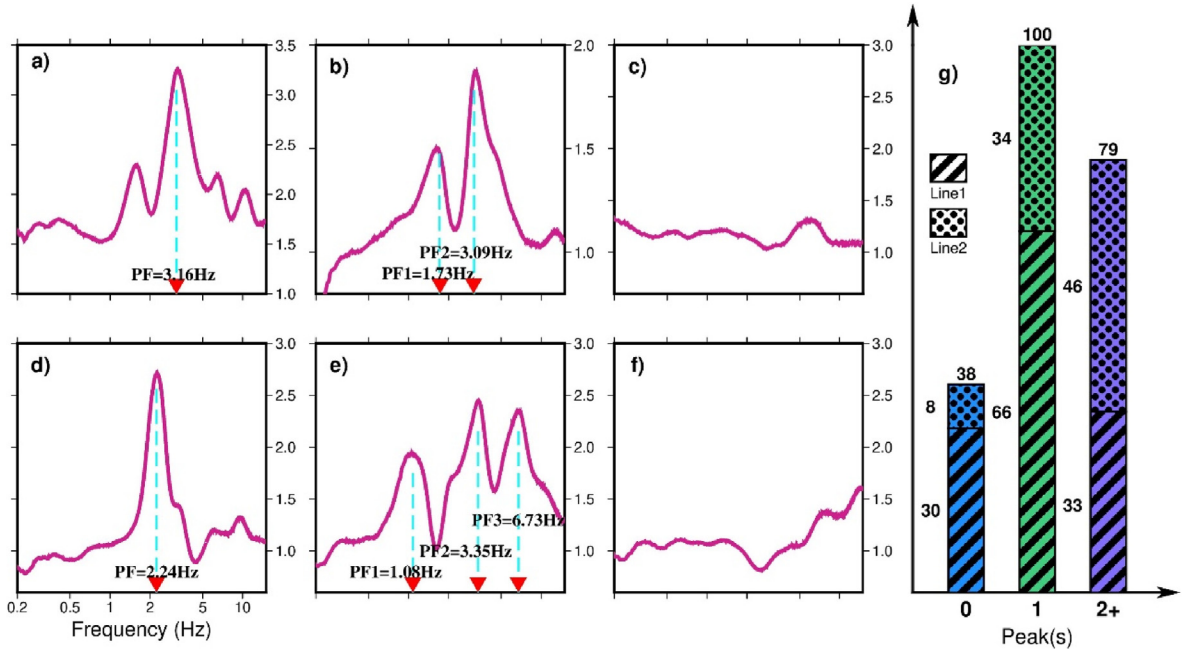

Fig. 3. Schematic diagram of the results and statistical analysis of various types of HVSR curves for all stations. (a), (b), (c) represents a typical single-peak, multi-peaks and no-peak HVSR curve in Line 1, respectively and (d), (e), (f) represents the HVSR curve of the same type but for Line 2. (g) Statistical plots of the peak number of all stations.

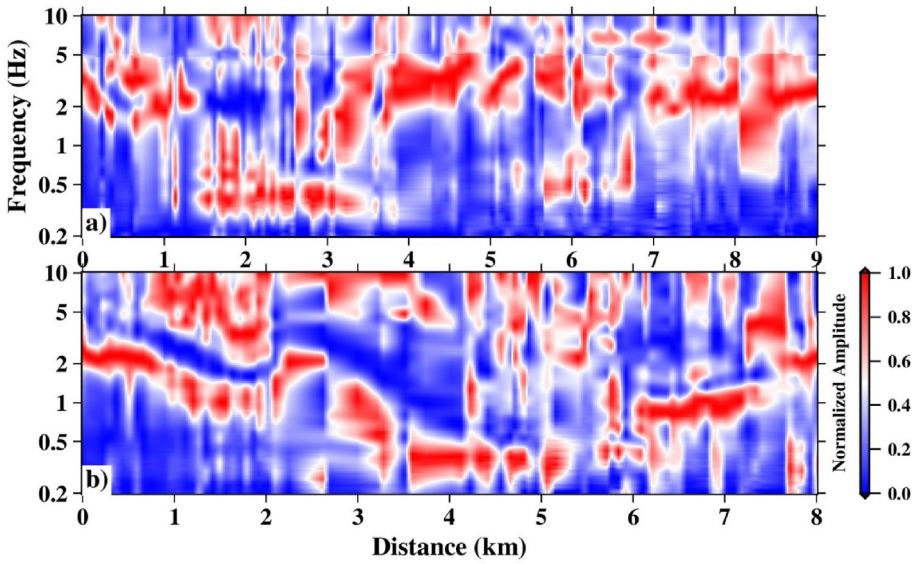

Fig. 4. Normalized HVSR (0.2–10 Hz) image along the profile with red indicating the peak frequency area. (a) and (b) represents the result of Line1 and Line2, respectively.

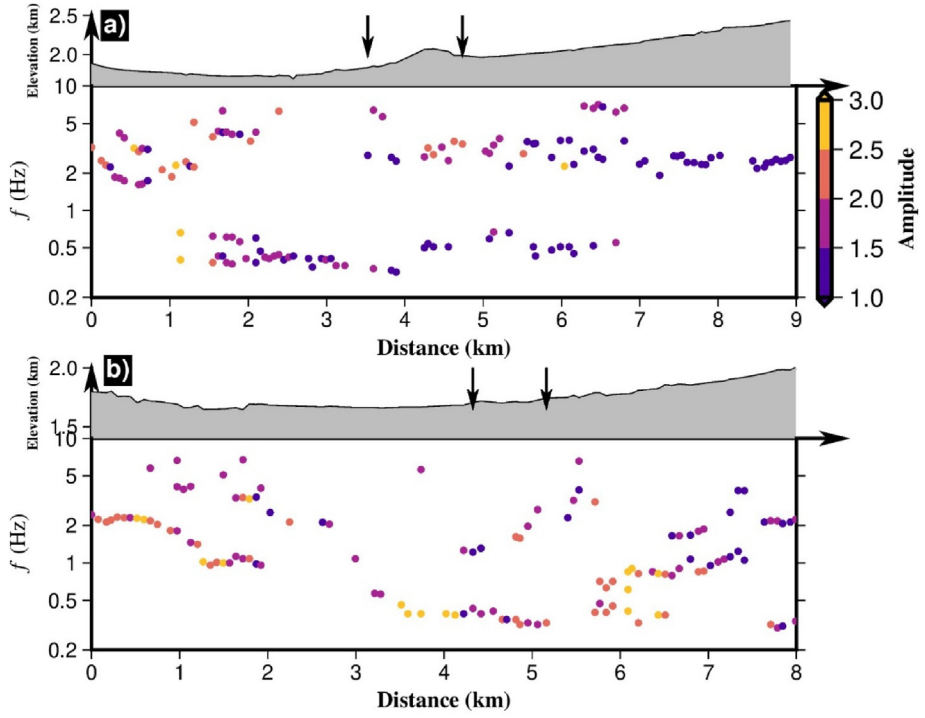

Fig. 5. Peak frequencies and peak amplitudes of HVSR curves for Line1 (a) and Line2 (b) with topography plotted above. The black arrows indicate the location where the Anninghe fault (two branches) passes through.

peak frequencies. When the stations across from the eastern branch of the Anninghe fault to the ending (5–8 km) were surrounded by mountains, the peak frequency increases to 2 Hz gradually and the amplitude is relatively small compared with other stations. By the way, there are some stations located at 6.5–7 km that show double peaks.

With the help of the quarter-wavelength method (Equas. 2-2) mentioned before, we converted the peak frequencies larger than 2 Hz to the depth domain under the assumption that the average S-wave velocity is about 250 m/s with 50 m/s uncertainty. At the same time, the exponential empirical relationship (Equas. 2-3) was used to convert the peak periods greater than 0.8s to the deeper interfaces. Combining the uncertainty of shallow S-wave velocities, the peak frequencies at 95% confidence intervals, and the different coefficients, the uncertainties of the converted depths can finally be carried out. Fig. 6a shows that the shallower sedimentary interface in Line 1 has a depth range of 10–40 m. A distinct depression appears at 1 km with a depth of about 30 m which is about 10 m deeper than the surroundings. We noticed that the shallow interface disappears at 2 km–3.5 km in the river valley and comes into our sight again from the west branch of the Anninghe fault to the end of Line 1. The deeper sedimentary interface is concentrated in the valley section through which the Anninghe flows (1–3 km) and the area through which the fracture zone passes (3–6 km). It should be noted that the

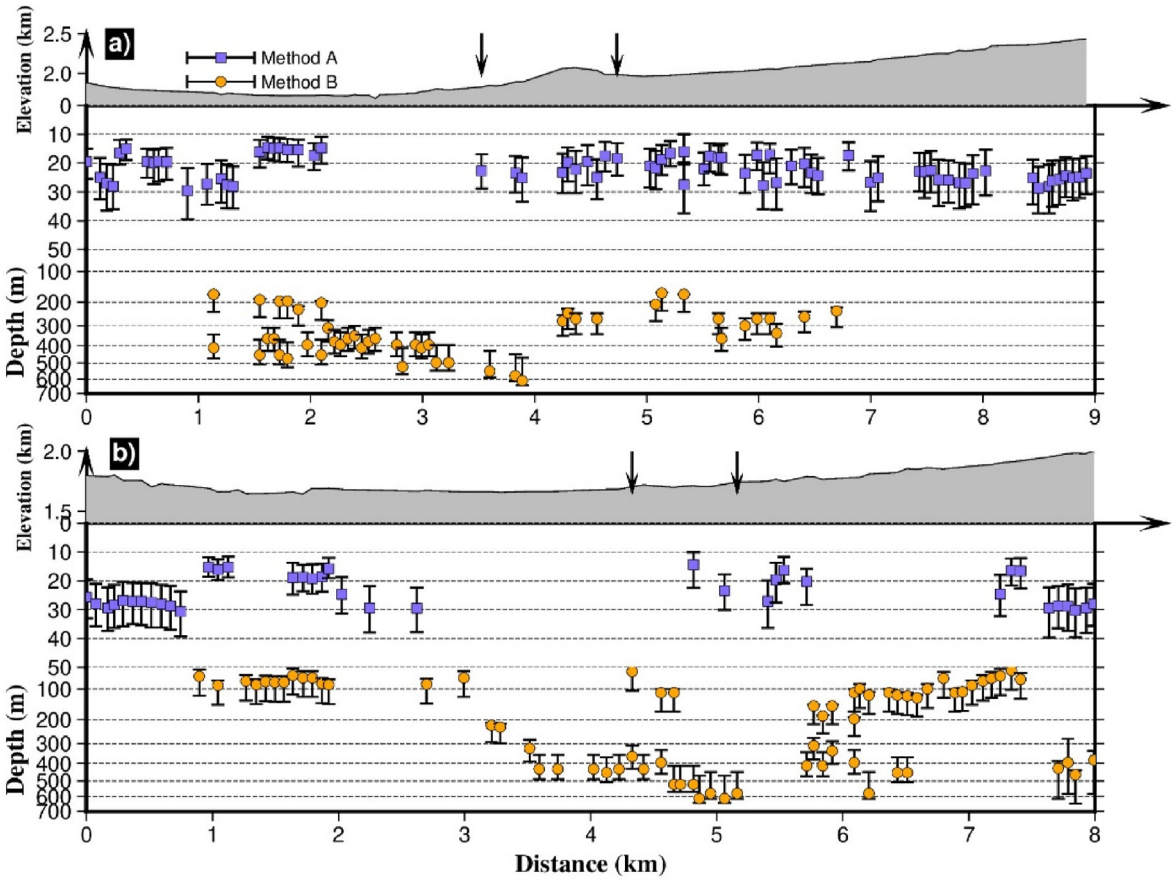

Fig. 6. Sedimentary interface depth with uncertainty derived from peak frequencies. (a) Sedimentary interface depth for Line 1. The slate-blue rectangles represent the depth converted by the quarter-wavelength method (Eqs. 2-2) while the orange circles represent the depth converted by the exponential relationship (Eqs. 2-3). Errorbar is derived from the average S-wave velocity (200–300 m/s), different coefficients, and ranges of peak frequencies within a 95% confidence interval. Black arrows represent the location where the Anninghe fault passes through. (b) The same as (a) but for Line 2. Note that the depth range of 0-50 m is plotted in a linear scale, while the range of 50-700 m is plotted in a logarithmic scale.

interface is in good continuity and deepening from both sides to the center (around 4 km) with a thickness ranging from 300 to 500 m. There are some differences in the geometry of the interface when it comes to Line 2 (Fig. 6b). Firstly, quite a large area misses the shallower sedimentary layer like 2.5–4.5 km and 6–7 km, and experiences really spatial variations in the fracture zone (around 5 km). However, the shallower interface becomes stable with a depth of 30 m on both sides which is dominated by mountains. Similar to Line 1, the deeper interface forms a V-like shape and the deepest position appears right beneath the Anninghe fault as well. According to the topography, we divided the deeper interface into three sections: the first part is the area where the Anninghe flows through (1–2 km) and the sediment interface is quite flat with a thickness of 100 m. The second section is the fracture zone (3–5 km) where the sediment interface begins to dip to the east. Like the first part, the last segment of the deeper sedimentary interface exists beneath a depression region on the east (6–7 km) with an average thickness of 150 m.

4. Discussion

4.1. Relationship between HVSR, lithology, and velocity

It is generally believed that the Anninghe fault originated in the Precambrian (He and Yasutakyr, 2007) and experienced the Jinning movement and Chengjiang orogeny. Multiple episodes of compression and extension activities during the Paleozoic and Mesozoic resulted in the development of magmatic complex belts along the fault zone (Wang et al., 1998; Ren, 2014). After the Cenozoic, the Himalayan movement gradually spread to the Sichuan-Yunnan region from north to south, leading to the asymmetry of the Anninghe Valley. The eastern side is much flatter compared with the west and a terrace with a width of 0.7 km–3 km developed between two branching faults (He and Yasutakyr, 2007). Geological investigations show that the lithology in the study area is complex including the magmatic rocks, metamorphic rocks, and sedimentary rocks (Fig. 7a). Combined with the shallow P-wave velocity model of this region obtained by Shao et al. (2022), the relationship between them is discussed as follows.

As we can observe that most of the stations in Line 1 are on the Quaternary sedimentary rocks (Fig. 7b) except the central part which is 1 km long and covered by the Sinian granite. Nonetheless, from the westernmost side to Hongxing Village (at about 102°10′30″) belongs to the diluvium which is composed mainly of gravel and sandstones. The P-wave velocity model shows that the shallow subsurface velocity in this area exceeds 5 km/s which is much higher than the other part. One possible explanation is that the sediment is relatively thin while the bedrock appears at a shallow depth, which can also account for the single peak of HVSR at the shallow position. In contrast, the section from Hongxing Village to Lianghekou (about 102°12′) belongs to the alluvium which is dominated by small gravel and sub-sandy soils and we can see there is an obvious low-velocity zone at the shallow surface of this section, suggesting that the area is rich in sedimentation. Multiple peaks are observed and a continuous and thick wave impedance interface can be inferred from the HVSR results. The stations on the Sinian rock topographically correspond to the Wojia mountain and the rocks are mainly

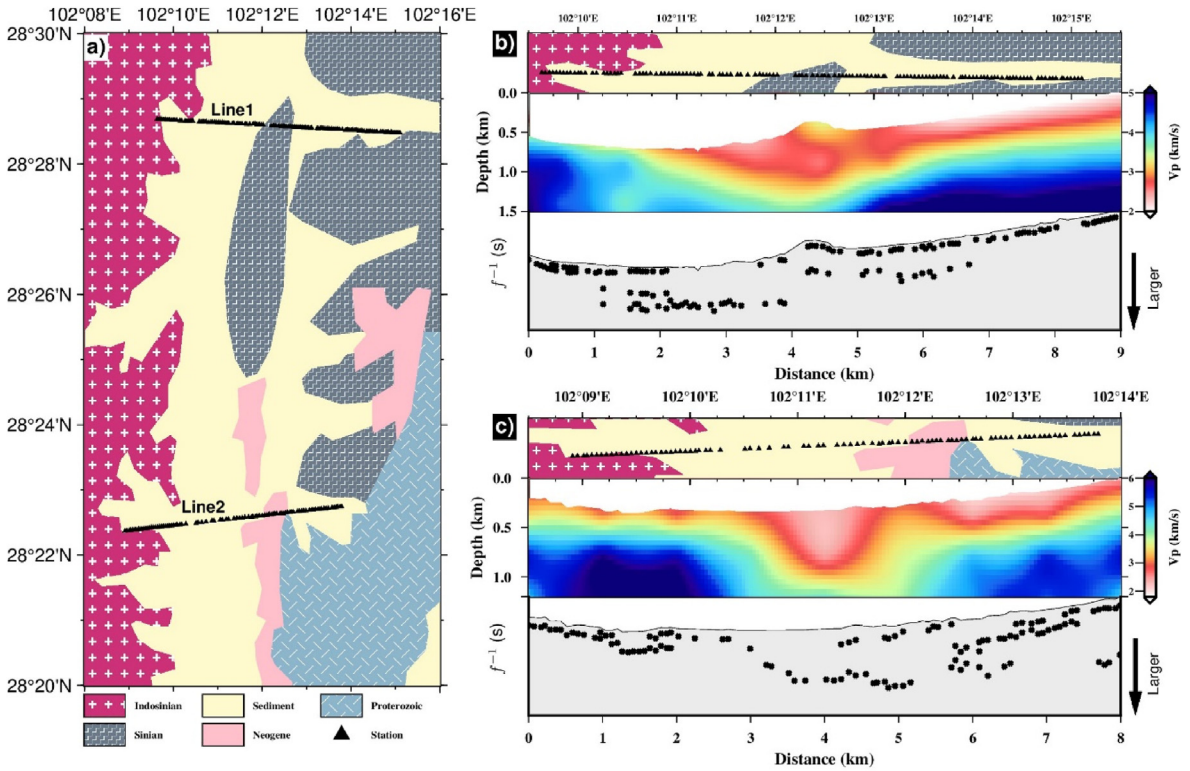

Fig. 7. Lithology distribution of the study area (a) and its comparison with the peak periods (the reciprocal of the peak frequency) and velocity map (b, c). The lithology results are modified from Luo (2019) and Yang et al. (2021) and the velocity model is obtained by Shao et al. (2022). The black triangles represent the stations and the peak periods in panels (b) and (c) are multiplied by a factor to fit the topography with a black arrow indicating the larger value.

rhyolite and a little volcanic clastic, resulting in another interface apart from the shallower one in this section. Peak frequencies change a little from Wojia mountain to the end of Line 1 except for stations located at 5–7 km whose HVSR curves have multiple peaks. Although the lithology is the same, the depression at around 6 km might be the reason for the multi-peaks phenomena which is revealed by the velocity model as well.

The first 1 km of Line 2 is located on Indochinese magmatic rocks (Fig. 7c) and a clear single-peak can be seen in Fig. 7c. Besides, a shallow sedimentary interface is indicated by the short value of the peak period (the reciprocal of peak frequency). The depression at 1.2 km in the velocity map also can be observed at the same position in the HVSR results. As the stations move eastward to the Anninghe valley which is mainly covered by Quaternary sediment, the peak frequency becomes smaller which indicates the thickness of sediment goes larger and forms an inverted trapezoid shape, corresponding to the terrane structure mentioned in He and Yasutakyr (2007). When the station passes through the Neoproterozoic Xigeda rocks whose density is larger than sedimentary rock but less than bedrock (Luo, 2019), the HVSR shows a single peak with an estimated thickness of about 40 m (Fig. 6) which is close to the 40–70 m thickness provided by geological data (Wang et al., 1998). As for the easternmost section of the line which is located on the Quaternary sedimentary rocks, the HVSR indicates a clear sedimentary interface which is supported by the existence of a large continuous low-velocity anomaly in the velocity model (Shao et al., 2022). In addition, the peak period decreases which means the sediment starts to become shallower as the stations extend to the mountain area.

Overall, the interface depicted by the HVSR exhibits a strong correlation with the local lithology and fits the velocity model obtained by Shao et al. (2022). We note that the peak H/V amplitudes of stations located in mountainous areas or magmatic rocks generally have a larger value (H/V $>$ 2, e.g., Wojia mountain area in the middle of Line 1). In contrast, this value drops to 1.5 when it comes to the Quaternary sedimentary rocks (e.g., the easternmost side of Line 1) except for the regions that have quite a thick sediment. This phenomenon suggests that information about the lithology and wave impedance of the rocks beneath the station may be contained in the peak frequency and amplitude.

4.2. Sediment around the fault fracture zone

HVSR results demonstrate that both lines show a continuous low-frequency peak near the valley area and where the Anninghe fault passes, with an average frequency of 0.5 Hz which most likely corresponds to a deep interface with significant impedance contrast. Unfortunately, the quarter-wavelength method fails in this situation due to large uncertainty in the average S-wave velocity estimate. Thus, the exponential relationship (Equas. 2-3) was exploited to convert the peak frequency below 0.55 Hz near the fracture zone to the depth domain. Different researchers give different coefficients based on the lithology of their study area which is shown in Fig. 8a and the coefficients proposed by Ibs-von Seht and Wohlenberg (1999) and Tun et al. (2016) were adopted in this study owing to the lithologies in our research areas are quite similar which are dominated by Quaternary to Tertiary rocks. In addition, a set of coefficients obtained by Wang et al. (2011) in the China region was also employed and Fig. 8b and c shows the final converted results.

The results obtained from the three sets of coefficients are generally consistent, with the interface depth difference within 100 m and the errors caused by the uncertainty of the peak frequency can be ignored when the depth is shallower than 400 m. Sedimentary thickness in the neighborhood of the fracture zone varies from 300 to 600 m and even exceeds 600 m in the central region. According to the results of the two lines, the characteristics of sediment near the fracture zone can be summarized as follows. Firstly, there is a sedimentary interface with a depth of about 400 m beneath the Anninghe fault zone and extends at least 2 km in the direction of the line. Secondly, there are differences between the two sides separated by the Anninghe fault. The west is

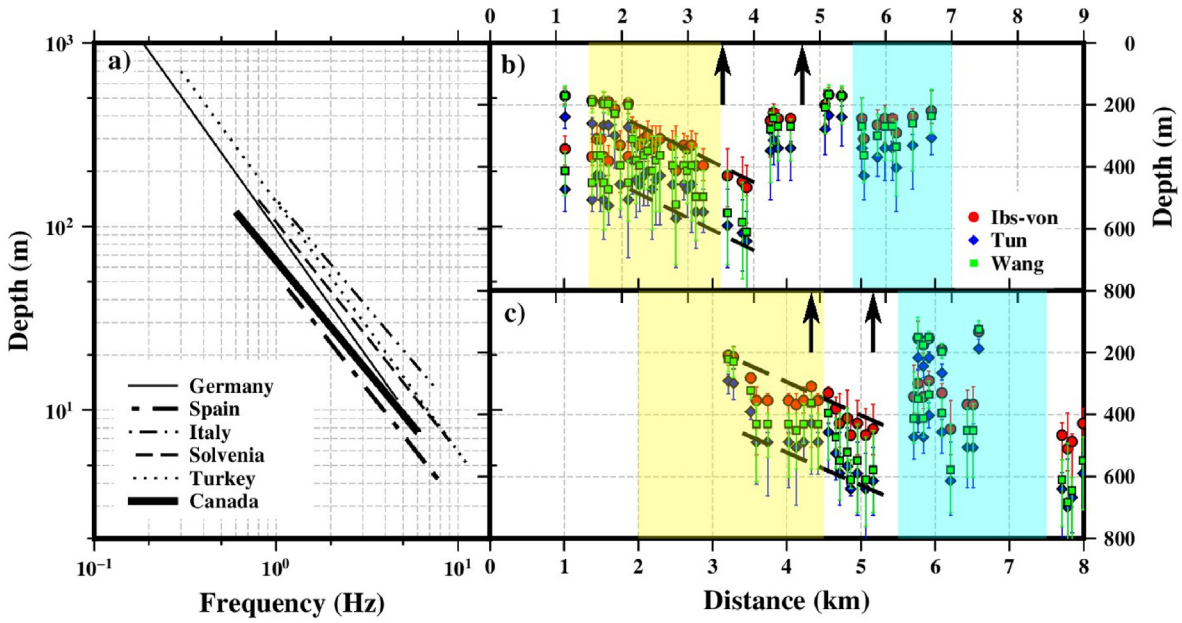

Fig. 8. Schematic diagram of the empirical relationship and converted interface depth in the vicinity of the fracture zone. (a) Different empirical relationships for Equas. (2-3) derived in various regions (Modified from Molnar et al. (2022)). (b) Converted depth of Line1 with uncertainty by adopting three sets of coefficients mentioned above. Yellow and cyan blocks highlight the Anninghe Valley and mountain valley, respectively. Black arrows indicate the location of the Anninghe fault. (c) The same as (b) but for Line 2.

slightly deeper than the east, especially for Line 1 where the differences reach 100 m, which is largely explained by the topography. While the Anninghe passes through the west and brings in abundant deposits like soil and sandstones, the eastern side is an ascending valley lacking sedimentary materials, which is also confirmed by the velocity model (Shao et al., 2022). Finally, the geometry of the sediment interface shows a downward dip to the east, which may be related to the east-west extrusion during the formation of the fault. Below the position where the fault passes, the sedimentary interfaces of the two lines are not positive 'V'-shaped, but slightly inclined to the west, indicating that the deep part has been pushed eastward. This shape is also consistent with the current understanding that the western branch of the Anninghe fault has the thrust component to the west (Ren, 2014).

4.3. Seismic resistance of buildings

Peak frequency can provide an important reference for the seismic vulnerability of buildings (Zhang et al., 2015; Chen et al., 2016; Guven, 2022). There are many villages with dense populations along the valley of the Anninghe fault and many people live in 2- to 3-story bungalows, most of which are relatively old and have limited earthquake resistance. Studies have shown that the resonance frequency of the low-block or masonry buildings in rural China is between 6 and 11 Hz (Zeng, 2012; Li, 2020; Zhou et al., 2020) while the self-oscillation period of 7- to 8-story

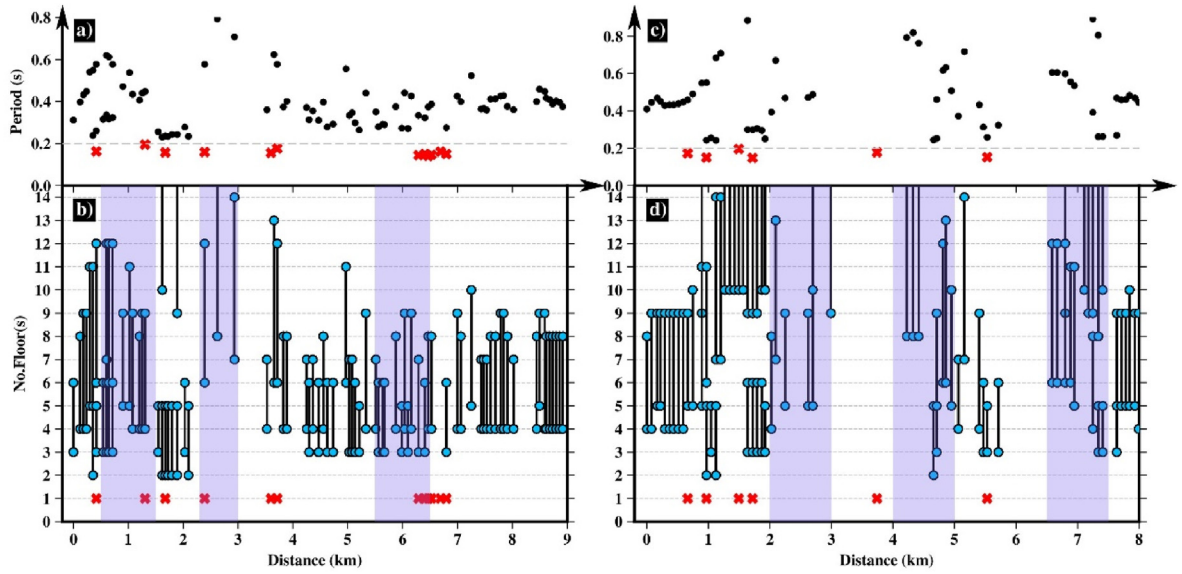

Fig. 9. The peak periods and the floor range of buildings which is prone to resonance based on Eqs. (4–1) along Line1 (a, b) and Line2 (c, d). Red crosses indicate the peak periods less than 0.2 s, which need extra attention. The blue circles show the error bar of the floor range and purple blocks highlight regions with dense populations.

old apartments is between 2.4 and 4 Hz (Huang et al., 2015). These buildings themselves are not strong in earthquake resistance. Together with their aging structures, they are extremely vulnerable to earthquake damage. According to the Code (2005) and Michel et al. (2010), the resonance frequency of mid- and high-rise concrete structures is represented as follows:

$$T = (0.05 \sim 0.1)n \tag{4-1}$$

where T and n represent the resonant period and the number of stories of the buildings, respectively.

The middle and high-rise buildings in the valley area are mainly schools, hospitals, and other infrastructure and some commercial buildings. These buildings are often densely populated and have higher requirements for structural earthquake resistance. We use Equas. (4-1) to figure out the upper and lower bound of the number of floors when the resonant frequency of the building matches the peak frequency of the sediment and Fig. 9 shows the results. It can be seen that in the densely populated areas (which are highlighted by purple blocks), the resonant period of the 6 to 9-story buildings is exactly in the range of the peak frequencies of the sedimentary layer, implying that these buildings are more vulnerable to earthquake damage (Bard, 1999). Some stations even show peak frequencies greater than 5 Hz (e.g. at 1.2 km, 2.4 km, and 6.2 km for Line1), where the low-rise buildings are also highly susceptible to seismic hazards. Based on the fact that the area is located in a seismic gap with significant strain accumulation (Wen et al., 2008a; Yang et al., 2021), some middle and high floors need regular checks and reinforcement.

5. Conclusions

In this study, we obtained the H/V spectral ratio and peak frequency profiles using two linear arrays deployed across the Anninghe fault zone between Mianning to the Xichang segment. Our results demonstrate that the peak frequency behaves highly correlated with lithology and is controlled by topography. The peak frequency is more continuous and stable in the foothills on both sides, mostly with a single peak of 2–3 Hz. While in the valley or the vicinity of the fracture zone, HVSR curves show the characteristics of multiple peaks, which may indicate the existence of a deeper sedimentary interface. Moreover, the HVSR is consistent with the previous studies like lithology and velocity which enhance the reliability of our results. With the aid of empirical relationships, the sediment depth and its uncertainty can finally be carried out. We proposed that the shallower sediment is around 10–30 m while the depth ranges from 300 to 600 m in the vicinity of valley and fracture zones. The geometry of the interface beneath the Anninghe fault indicates that it has experienced strong eastward stress which is supported by recent observations. Based on the HVSR results and resonant frequency of architecture, buildings of 6–9 stories need more attention especially the high locking depth and extent of the Anninghe fault is verified.

Declaration of competing interest

The authors declare that they have no known competing financial interests or personal relationships that could have appeared to influence the work reported in this paper.

Author agreement and Acknowledgments

The authors declare that the work described was original research that has not been published previously and is not under consideration for publication elsewhere, in whole or in part. All the authors listed have approved the manuscript that is enclosed. the authors are grateful to two anonymous reviewers and the editor for their constructive comments. Most figures were generated using Generic Mapping Tools (GMT; Wessel et al. (2013)). This study was jointly supported by the Key Research and Development Program of China (2021YFC3000704, 2018YFC1503400), the National Natural Science Foundation of China (42125401), the special fund of Key Laboratory of Earthquake Prediction, CEA (2021IEF0103).

Appendix

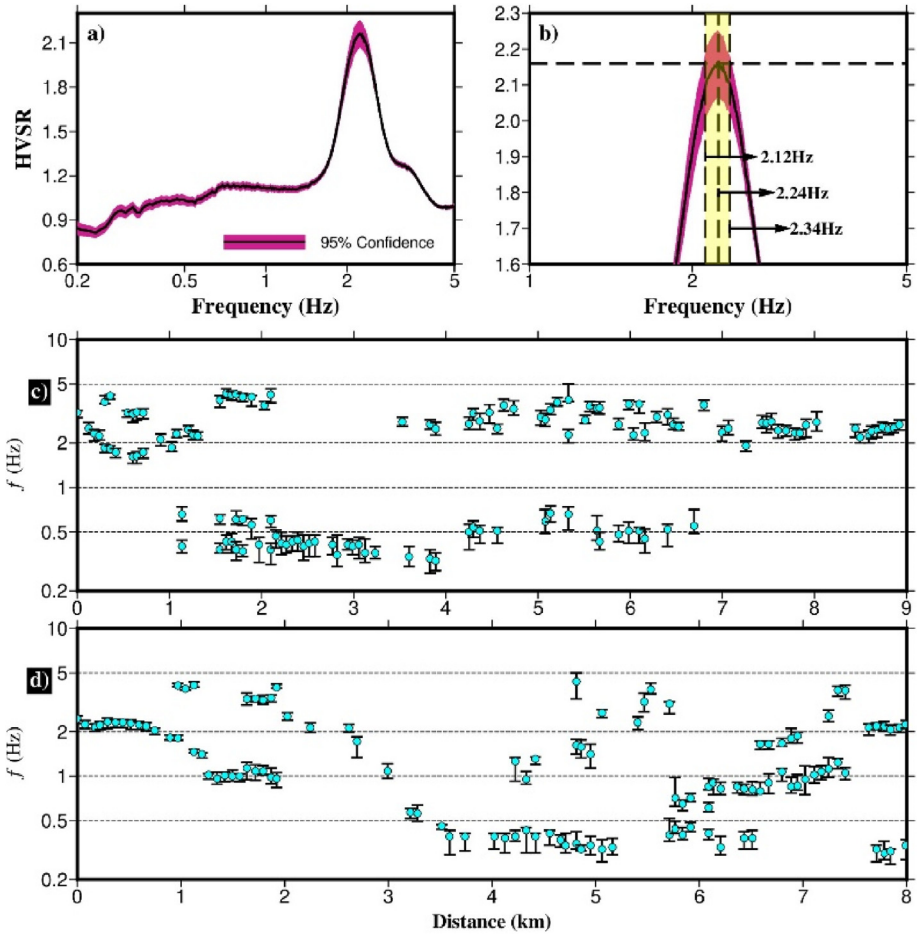

Fig. A 1. Schematic diagram of the uncertainty of the peak frequency derived from the statistical analysis. (a) HVSR curves together with its 95% confidence interval of station AL202. (b) Zoom in of (a) and yellow block represents the peak frequency interval whose peak amplitude might be larger than the amplitude of f_0. (c) Peak frequency uncertainty for all stations of Line1 obtained by the same way of (b). (d) The same as (c) but for Line2.

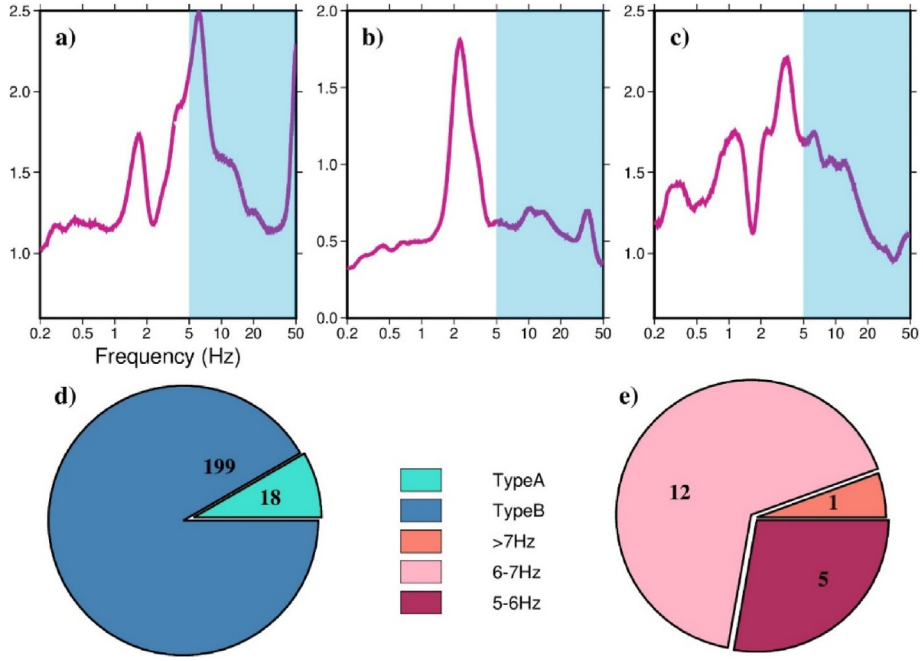

Fig. A 2. Plots of HVSR curves from 0.5 to 50 Hz for some stations and the statistical characteristics. (a), (b), and(c) represents the HVSR curve of stations AL008, AL022, and AL223, respectively. (d) Statistical plots showing the existence of peaks above 5 Hz (TypeA) and the lack of peaks above 5 Hz (TypeB). (e) Peak frequency distribution of TypeB. Based on the fact that most peak frequencies are within 10 Hz, only 0.2–10 Hz was plotted in this study.

References

Acerra, C., Aguacil, G., Anastasiadis, A., Atakan, K., Azzara, R., Bard, P.-Y., Basili, R., Bertrand, E., Bettig, B., Blarel, F., 2004. Guidelines for the Implementation of the H/V Spectral Ratio Technique on Ambient Vibrations Measurements, Processing and Interpretation. No. European Commission–EVG1-CT-2000-00026 SESAME. European Commission, Brussels, Belgium.

Bao, F., Li, Z., Yuen, D.A., Zhao, J., Ren, J., Tian, B., Meng, Q., 2018. Shallow structure of the Tangshan fault zone unveiled by dense seismic array and horizontal-to-vertical spectral ratio method. Phys. Earth Planet. In. 281, 46–54.

Bao, X., Sun, X., Xu, M., Eaton, D.W., Song, X., Wang, L., Ding, Z., Mi, N., Li, H., Yu, D., Huang, Z., Wang, P., 2015. Two crustal low-velocity channels beneath SE Tibet revealed by joint inversion of Rayleigh wave dispersion and receiver functions. Earth Planet Sci. Lett. 415, 16–24.

Bard, P.Y., 1999. Microtremor measurements: a tool for site effect estimation. The effects of surface geology on seismic motion 3, 1251–1279.

Bodin, P., Smith, K., Horton, S., Hwang, H., 2001. Microtremor observations of deep sediment resonance in metropolitan Memphis, Tennessee. Eng. Geol. 62 (1–3), 159–168.

Chen, Y., Huang, H., Wu, C., 2016. Site-effect estimations for Taipei Basin based on shallow S-wave velocity structures. J. Asian Earth Sci. 117, 135–145.

Chen, Z., Burchfiel, B.C., Liu, Y., King, R.W., Royden, L.H., Tang, W., Wang, E., Zhao, J., Zhang, X., 2000. Global Positioning System measurements from eastern Tibet and their implications for India/Eurasia intercontinental deformation. J. Geophys. Res. Solid Earth 105 (B7), 16215–16227.

Code, P., 2005. Eurocode 8: Design of Structures for Earthquake Resistance-Part 1: General Rules, Seismic Actions and Rules for Buildings. European Committee for Standardization, Brussels.

Guven, I.T., 2022. Seismic vulnerability indices for ground in Derince-Kocaeli (NW Turkey). Environ. Earth Sci. 81 (5).

He, H., Yasutakyr, I., 2007. Faulting on the Anninghe fault zone, southwest China in late Quaternary and its movement model(in Chinese). Acta Seismologica Sinica 29 (5), 537–548.

Hu, J., Badal, J., Yang, H., Li, G., Peng, H., 2018. Comprehensive crustal structure and seismological evidence for lower crustal flow in the southeastern margin of Tibet revealed by receiver functions. Gondwana Res. 55, 42–59.

Hu, P., Luo, Y., Song, Z., Nan, K., 2022. H/V spectral ratio characteristics of hidden fault site based on ambient noise test(in Chinese). Acta Seismologica Sinica 44 (3), 528–537.

Huang, B., Xia, T., Zhao, Q., He, P., 2015. Vibration reduction for brick-concrete buildings in a old residential area(in Chinese). China Earthquake Engineering Journal 37 (1), 126–130.

Ibs-von Seht, M., Wohlenberg, J., 1999. Microtremor measurements used to map thickness of soft sediments. Bull. Seismol. Soc. Am. 89 (1), 250–259.

Jones, J.P., van der Baan, M., 2015. Adaptive STA-LTA with outlier statistics. Bull. Seismol. Soc. Am. 105 (3), 1606–1618.

King, R.W., Shen, F., Burchfiel, B.C., Royden, L.H., Wang, E.C., Chen, Z.L., Liu, Y.P., Zhang, X.Y., Zhao, J.X., Li, Y.L., 1997. Geodetic measurement of crustal motion in southwest China. Geology 25 (2), 179–182.

Konno, K., Ohmachi, T., 1998. Ground-motion characteristics estimated from spectral ratio between horizontal and vertical components of microtremor. Bull. Seismol. Soc. Am. 88 (1), 228–241.

Lachet, C., Bard, P.Y., 1994. Numerical and theoretical investigations on the possibilities and limitations of Nakamura technique. J. Phys. Earth 42 (5), 377–397.

Li, C., Yao, H., Fang, H., Huang, X., Wan, K., Zhang, H., Wang, K., 2016. 3D near-surface shear-wave velocity structure from ambient-noise tomography and borehole data in the hefei urban area, China. Seismol Res. Lett. 87 (4), 882–892.

Li, L., 2020. Seismic Capacity Analysis and Earthquake Damage Prediction of Rural Houses in Chaganhua Earthquake Area of Songyuan City. Master Thesis, Institute of Engineering Mechanics, China Earthquake Administration.

Liu, Q., van der Hilst, R.D., Li, Y., Yao, H., Chen, J., Guo, B., Qi, S., Wang, J., Huang, H., Li, S., 2014. Eastward expansion of the Tibetan Plateau by crustal flow and strain partitioning across faults. Nat. Geosci. 7 (5), 361–365.

Liu, Y., Yao, H., Zhang, H., Fang, H., 2021. The community velocity model V.1.0 of Southwest China, constructed from joint body- and surface-wave travel-time tomography. Seismol Res. Lett. 92 (5), 2972–2987.

Luo, F., 2019. Landslide Development Characteristics and Hazard Assessment of Mianning–Xichang Section of Anning River(in Chinese). Master Thesis. Chengdu University of Technology, Chengdu.

Luo, S., Yao, H., Wen, J., Yang, H., Tian, B., Yan, M., 2023. Apparent low-velocity belt in the shallow Anninghe fault zone in SW China and its implications for seismotectonics and earthquake hazard assessment. J. Geophys. Res. Solid Earth, e2022JB025681.

Michel, C., Gueguen, P., Lestuzzi, P., Bard, P.Y., 2010. Comparison between seismic vulnerability models and experimental dynamic properties of existing buildings in France. Bull. Earthq. Eng. 8 (6), 1295–1307.

Mokhberi, M., 2015. Vulnerability evaluation of the urban area using the H/V spectral ratio of microtremors. Int. J. Disaster Risk Reduc. 13, 369–374.

Molnar, S., Sirohey, A., Assaf, J., Bard, P.Y., Castellaro, S., Cornou, C., Cox, B., Guillier, B., Hassani, B., Kawase, H., Matsushima, S., Sanchez-Sesma, F.J., Yong, A., 2022. A review of the microtremor horizontal-to-vertical spectral ratio (MHVSR) method. J. Seismol. 26 (4), 653–685.

Nakamura, Y., 1989. A method for dynamic characteristics estimation of subsurface using microtremor on the ground surfac. Quarterly Report of RTRI 30 (1).

Panou, A.A., Theodulidis, N., Hatzidimitriou, P., Stylianidis, K., Papazachos, C.B., 2005. Ambient noise horizontal-to-vertical spectral ratio in site effects estimation and correlation with seismic damage distribution in urban environment: the case of the city of Thessaloniki (Northern Greece). Soil Dynam. Earthq. Eng. 25 (4), 261–274.

Ren, Z., 2014. Late quaternary deformation features along the Anninghe fault on the eastern margin of the Tibetan plateau. J. Asian Earth Sci. 85, 53–65.

Shao, X., Yao, H., Liu, Y., Yang, H., Tian, B., Fang, L., 2022. Shallow crustal velocity structures revealed by active source tomography and fault activities of the Mianning-Xichang segment of the Anninghe fault zone, Southwest China. Earth and Planetary Physics 6 (2), 204–212.

Tun, M., Pekkan, E., Ozel, O., Guney, Y., 2016. An investigation into the bedrock depth in the Eskisehir Quaternary Basin (Turkey) using the microtremor method. Geophys. J. Int. 207 (1), 589–607.

Vassallo, M., Cultrera, G., Di Giulio, G., Cara, F., Milana, G., 2022. Peak frequency changes from HV spectral ratios in Central Italy: effects of strong motions and seasonality over 12 Years of observations. J. Geophys. Res. Solid Earth 127 (5).

Wang, W., Chen, Q., Qi, C., Tan, Y., Zhang, X., Zhou, Q., 2011. The feasibilities and limitations to explore the near-surface structure with microtremor HVSR method- A case in baoding area of Hebei Province, China. Chinese Journal of Geophysics-Chinese Edition 54 (7), 1783–1797.

Wang, X., Zhang, C., Pei, X., 1998. Structural activity and evolution since the late quaternary on Anninghe faults(in Chinese). Earthq. Res. China 98 (4), 1–12.

Wen, X., 2000. Character of rupture segmentation of the Xianshuihe-Anninghe-Zemuhe fault zone, western Sichuan(in Chinese). Seismol. Geol. 22 (3), 239–249.

Wen, X., Fan, J., Yi, G., Deng, Y., Long, F., 2008a. A seismic gap on the Anninghe fault in western Sichuan, China(in Chinese). Sci. China Earth Sci. 51 (10), 1375–1387.

Wen, X., Ma, S., Lei, X., Nishizawa, Y., Kiguchi, T., Chen, Q., 2007. Newly found surface rupture remains of largehistorical earthquakes on and near the transitionsegment of the Anninghe and Zemuhe fault zones, western Sichuan, China(in Chinese). Seismol. Geol. 29 (4), 826–833.

Wen, X., Ma, S., Xu, X., He, Y., 2008b. Historical pattern and behavior of earthquake ruptures along the eastern boundary of the Sichuan-Yunnan faulted-block, southwestern China. Phys. Earth Planet. In. 168 (1–2), 16–36.

Wessel, P., Smith, W.H.F., Scharroo, R., Luis, J., Wobbe, F., 2013. Generic mapping tools: improved version released. Eos, Transactions American Geophysical Union 94 (45), 409–410.

Xu, L., Rondenay, S., van der Hilst, R.D., 2007. Structure of the crust beneath the southeastern Tibetan Plateau from teleseismic receiver functions. Phys. Earth Planet. In. 165 (3–4), 176–193.

Yang, Y., Li, Y., Li, Y., Ji, L., Gong, Y., Du, F., Zhang, L., Chen, Z., 2021. Present-day activity of the Anninghe fault and Zemuhe fault, southeastern Tibetan plateau, derived from soil gas CO2 emissions and locking degree. Earth Space Sci. 8 (10).

Yang, Y., Yao, H., Wu, H., Zhang, P., Wang, M., 2020. A new crustal shear-velocity model in Southwest China from joint seismological inversion and its implications for regional crustal dynamics. Geophys. J. Int. 220 (2), 1379–1393.

Yao, H., Beghein, C., van der Hilst, R.D., 2008. Surface wave array tomography in SE Tibet from ambient seismic noise and two-station analysis - II. Crustal and upper-mantle structure. Geophys. J. Int. 173 (1), 205–219.

Yao, H., van der Hilst, R.D., de Hoop, M.V., 2006. Surface-wave array tomography in SE Tibet from ambient seismic noise and two-station analysis - I. Phase velocity maps. Geophys. J. Int. 166 (2), 732–744.

Zeng, Y., 2012. Finite Element Analysis of the Towns and Villages Wooden Framed House Reinforcement Model. Master Thesis. Hebei University of Technology.

Zhang, H., Xu, J., Chen, Z., 2015. Site response of Fujian seismic monitoring stations based on Nakamura H/V spectral ratio method(in Chinese). Acta Seismologica Sinica 37 (6), 1045–1058.

Zhang, P., 2008. The current state of the tectonic deformation, strain distribution, and deep dynamic processes in the western Sichuan region, eastern margin of the Tibetan Plateau(in Chinese). Sci. China Earth Sci. 38 (9), 1041–1056.

Zhang, P., Shen, Z., Wang, M., Gan, W., Burgmann, R., Molnar, P., 2004. Continuous deformation of the Tibetan Plateau from global positioning system data. Geology 32 (9), 809–812.

Zhang, Z., Yao, H., Yang, Y., 2020. Shear wave velocity structure of the crust and upper mantle in Southeastern Tibet and its geodynamic implications. Sci. China Earth Sci. 63 (9), 1278–1293.

Zhang, Z., Yuan, X., Chen, Y., Tian, X., Kind, R., Li, X., Teng, J., 2010. Seismic signature of the collision between the east Tibetan escape flow and the Sichuan Basin. Earth Planet Sci. Lett. 292 (3–4), 254–264.

Zhou, X., Yao, X., Guan, Y., Shi, Y., 2020. Influence analysis of different structural parameters on seismic performance of low-rise lightweight steel buildings. Journal of Hunan University(Natural Sciences) 47 (1), 1–9.

Zhu, J., Chen, G., Xu, H., Liu, X., 2018. Spatial variation characteristics of shear wave velocity structure and its application to quaternary deep sediment layers in Suzhou region. Chin. J. Geotech. Eng. 40 (4), 726–735.